A 3.1-5.2GHz, Energy-Efficient Single Antenna, Cancellation-Free, Bitwise Time-Division Duplex Transceiver for High Channel Count Optogenetic Neural Interface

Yu-Ju Lin, Hyunsoo Song, *Graduate Student Member, IEEE*, Sungjin Oh, *Graduate Student Member, IEEE*, Mihály Vöröslakos, Kanghwan Kim, *Member, IEEE*, Xing Chen, *Member, IEEE*, David D. Wentzloff, *Senior Member, IEEE*, György Buzsáki, Sung-Yun Park, *Member, IEEE*, and Euisik Yoon, *Fellow, IEEE*

***Abstract*—We report an energy-efficient, cancellation-free, bitwise time-division duplex (B-TDD) transceiver (TRX) for real-time closed-loop control of high channel count neural interfaces. The proposed B-TDD architecture consists of a duty-cycled ultra-wide band (UWB) transmitter (3.1−5 GHz) and a switching U-NII band (5.2 GHz) receiver. An energy-efficient duplex is realized in a single antenna without power-hungry self-interference cancellation circuits which are prevalently used in the conventional full-duplex, single antenna transceivers. To suppress the interference between up- and down-links and enhance the isolation between the two, we devised a fast-switching scheme in a low noise amplifier and used 5× oversampling with a built-in winner-take-all voting in the receiver. The B-TDD transceiver was fabricated in 65 nm CMOS RF process, achieving low energy consumption of 0.32 nJ/b at 10 Mbps in the receiver and 9.7 pJ/b at 200 Mbps in the transmitter, respectively. For validation, the B-TDD TRX has been integrated with a μLED optoelectrode and a custom analog frontend integrated circuit in a prototype wireless bidirectional neural interface system. Successful *in-vivo* operation for simultaneously recording broadband neural signals and optical stimulation was demonstrated in a transgenic rodent.**

***Index Terms*—Bit-wise time-division duplex (B-TDD), transceiver (TRX), closed-loop control, ultra-wide band (UWB), unlicensed national information infrastructure (U-NII) band, wireless neural interface.**

Manuscript received September 29, 2021; revised November 23, 2021 and December 22, 2021; accepted December 24, 2021. Date of publication January 4, 2022; date of current version May 9, 2022. This work was supported in part by NSF under Grants 1545858 and 1707316, and in part by NIH under Grant 1RF1NS113283-01. This paper was recommended by Associate Editor R. Rieger. *(Corresponding authors: Sung-Yun Park; Euisik Yoon).*

Yu-Ju Lin, Hyunsoo Song, Sungjin Oh, Xing Chen, and David D. Wentzloff are with the Center for Wireless Integrated MicroSensing and Systems (WIMS2), Department of Electrical Engineering and Computer Science, University of Michigan, Ann Arbor, MI 48109 USA (e-mail: yujulin@umich.edu; hyunsoos@umich.edu; sngjnoh@umich.edu; chenxing@umich.edu; wentzlof@umich.edu).

Mihály Vöröslakos is with the Center for Wireless Integrated MicroSensing and Systems (WIMS2), Department of Electrical Engineering and Computer Science, University of Michigan, Ann Arbor, MI 48109 USA, and also with New York University, NY 10012 USA (e-mail: mvoeroes@umich.edu).

Kanghwan Kim is with the Center for Wireless Integrated MicroSensing and Systems (WIMS2), Department of Electrical Engineering and Computer Science, University of Michigan, Ann Arbor, MI 48109 USA, and also with the Korea Institute of Science and Technology, Seoul 02792, Korea (e-mail: khankim@umich.edu).

György Buzsáki is with the New York University, NY 10012 USA (e-mail: gyorgy.buzsaki@nyulangone.org).

Sung-Yun Park is with the Center for Wireless Integrated MicroSensing and Systems (WIMS2), Department of Electrical Engineering and Computer Science, University of Michigan, Ann Arbor, MI 48109 USA, and also with the Department of Electronics Engineering, Pusan National University, Busan 43241, Korea (e-mail: sungyun@umich.edu).

Euisik Yoon is with the Center for Wireless Integrated MicroSensing and Systems (WIMS2), Department of Electrical Engineering and Computer Science, University of Michigan, Ann Arbor, MI 48109 USA, and also with the Center for Nanomedicine Institute for Basic Science (IBS) and Graduate Program of Nano Biomedical Engineering (Nano BME), Advanced Science Institute, Yonsei University, Seoul 03722, Korea (e-mail: esyoon@umich.edu).

Color versions of one or more figures in this article are available at https://doi.org/10.1109/TBCAS.2021.3139891.

Digital Object Identifier 10.1109/TBCAS.2021.3139891

I. Introduction

Optogenetics is one of the most essential tools for neuroscience research since its first inception in 2005 [1]. With this technique, genetically modified neuronal activities can be excited or inhibited through optical stimulation at a specific wavelength. This cell type specificity ensures higher spatial resolution than the traditional methods such as electrical or ultrasonic stimulations [2]. To relate specific neural patterns of individual neurons to behavioral or cognitive variables, electrophysiological recordings should be combined with optogenetic simulation [3], [4]. In order to implement a fully bidirectional optogenetic neuromodulation system, many design criteria must be concurrently fulfilled, including high-bandwidth signal recording from a massive number of neurons and precise temporal control of multiple optical stimulation sites. In addition, the implantable system must be integrated in a small form factor and light weight, while restricted by low power consumption and heat dissipation. More specifically, the total system weight, including power sources, assembly cables, passive components, and any interconnections, should be less than 5-gram for free-behaving animal tests in rodents such as rats [5].

Another essential prerequisite for the optogenetic neuromodulation system is a wireless data telemetry because it enables behavioral studies among multiple freely moving subjects without restrictions involved by cable tangling as well as eliminates tethering problems of the animals under test [6]–[8]. According to recent literatures [9]–[12], the key requirements for the wireless telemetry for neural interfaces are: 1) high data bandwidth to facilitate the growing demands for high channel-count requirement; 2) low power consumption due to scarce power sources and temperature rise restriction for living tissues [13]; and 3) small footprint for the consideration of longevity of implantable neural interfaces, while embedding 4) duplex functionality for closed-loop modulations. In particular, the recent demand for high channel-count neural interface has pushed the requirement in data bandwidth [14]–[20] aggressively. For uplink, the data rate easily exceeds a few hundred Mbps if the recording channel count becomes larger than 100 [16]–[20]. For downlink, a few 10s of kbps is sufficient as only short commands for simple channel adjustments are transmitted [9]. As closed-loop systems have been further developed, however, the higher channel count is also required in stimulation and the variables to manipulate stimulation patterns and to shape the waveforms have become complicated [4], [19], which demands a several Mbps downlink bandwidth. Current mainstream commercial chipsets such as Bluetooth low energy (BLE), although benefiting from its low power consumption, are not suitable due to its low uplink bandwidth and overdesigned downlink.

One of the most straightforward solutions to realize a full-duplex communication for real-time wireless data telemetry is to employ frequency division duplex (FDD) for receiving and transmitting using two separate antennas. Although it reduces the complexity for ASIC implementation [12], the system becomes bulky due to the footprint constraints not only for the antennas, but also for PCB routing; *i.e.*, the distance between the two antennas that needs to be met for interference cancellation directly correlated to signal wavelengths. As a result, FDD is not suitable for fully implantable applications where the system size needs to be minimized. To realize a compact wireless telemetry, Rajavi *et al.* adopted a surface acoustic wave (SAW) duplexer to provide high-Q bandpass filtering to two adjacent transmission frequency bands with only one antenna [10]. Since the duplexer provides only $\sim$50 dB of isolation between TX and RX, an extra cancellation scheme or isolation method is required for a large signal bandwidth. Aside from the isolation problem, the size of the duplexer itself is also 4$\times$ larger than the whole chip, which also makes it unsuitable for implantable applications. Instead of commercial off-the-shelf components (COTS), the on-chip signal self-interference cancellation (SIC) schemes either in the analog front-end or in digital circuits have been proposed [11], [21], but their high power consumption and the complexity make the scheme unacceptable for the target application.

In this paper, we report an energy-efficient bit-wise time-division duplex (B-TDD) wireless transceiver for real-time, high channel count, optogenetic neural interface. The proposed transceiver is suitable for freely behaving small animal studies *in vivo* because the duplex operation can be realized with a single antenna, resulting in a compact and high energy-efficient uplink/downlink at 9.7 pJ/b and 0.32 nJ/b, respectively. In addition, a fast-switching low noise amplifier (LNA) and a simple winner-take-all voting circuit have been implemented to achieve reliable operation by enhancing the isolation between up- and

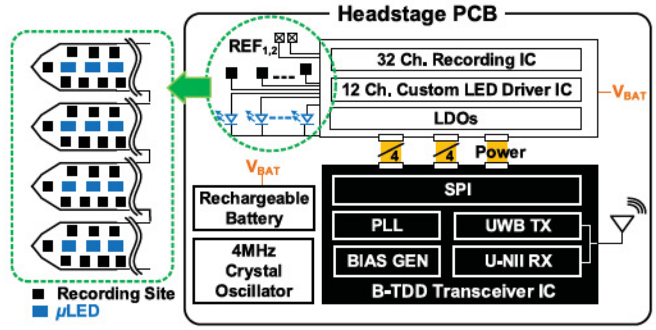

Fig. 1. Wireless optogenetic neural interface block diagram with the proposed B-TDD transceiver.

down-links. Unlike the conventional time division duplex (TDD) operation [22] where the data RX and TX cannot be simultaneously realized without dedicated memories, the proposed B-TDD scheme seamlessly sends and receives data with no storage place on- or off-chip. To verify the feasibility of the proposed B-TDD wireless transceiver *in vivo*, the fabricated transceiver chip has been integrated in a prototype optogenetic wireless neural interface headstage where a custom bidirectional neural interface AFE circuit chip [19], an ultra-light rechargeable Li-battery, a micro-machined opto-electrode [4], [23], and a commercially available antenna are assembled, as shown in Fig. 1. The B-TDD transceiver can support up to 200 Mbps uplink and 10 Mbps downlink for simultaneous recording and stimulation, respectively. This allows for embracing up to >1000-channel broadband neural recording with 10-b resolution and >100-channel stimulation with 8-b stimulation waveform adjustment.

This paper is organized as follows. The working principle of the proposed B-TDD is introduced and the related circuit architecture is described in Section II. In Section III, the architecture of the proposed B-TDD transceiver is described. This section provides the detailed description of essential integrated circuit blocks used to realize the proposed B-TDD transceiver. The bench top and *in vivo* measurement results for the proposed transceiver and the prototype wireless bidirectional optogenetic interface are given in Section IV. Finally, Section V concludes the paper.

II. Bit-Wise Time-Division Duplex Transceiver

The one of the most essential parts for the wireless bi-directional neural interface to be used for the electrophysiology study with freely behaving small animals is the energy-efficient and compact (*e.g.*, having a single antenna) duplex transceiver. To realize an energy-efficient, cancellation-free, single-antenna solution for the duplex wireless transceiver, we devised the B-TDD operation by utilizing the duty-cycled operation of an UWB transmitter and a fast-switching receiver, as shown in Fig. 2. In the time domain, the UWB transmitter emits pulses in a very short duration, which frees up a time slot for receiving signals, as shaded light gray in Fig. 2(a). With a data rate of 200 Mbps, it gives "blank time space" which is almost 80% of a single TX time frame of 5 ns at the given the carrier

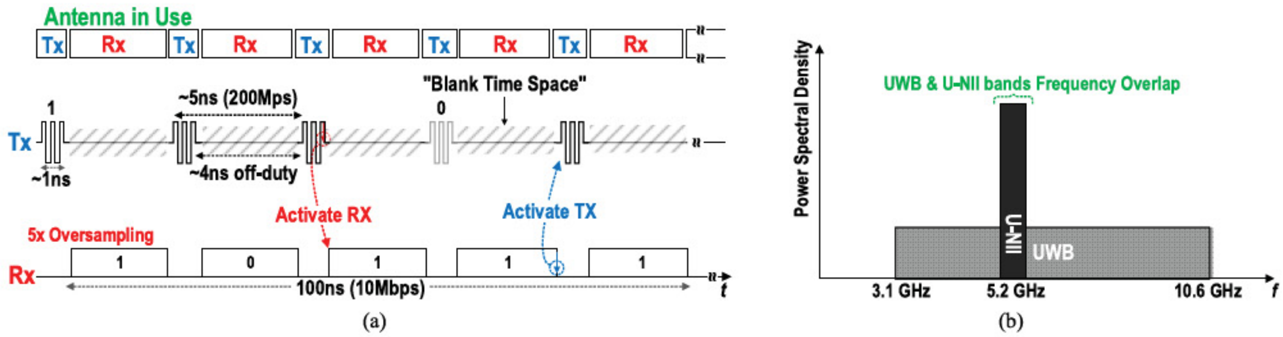

Fig. 2. Conceptual diagram for the waveform allocation in time domain (a), in frequency domain (b) in the proposed B-TDD architecture.

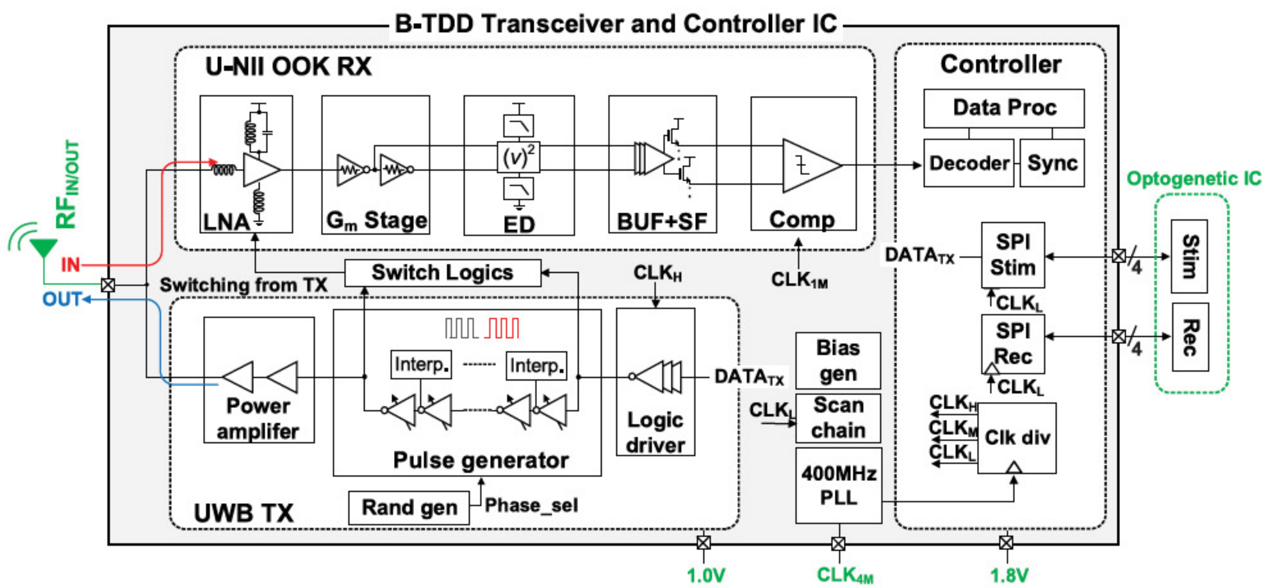

Fig. 3. Top level circuit architecture of the proposed cancellation-free B-TDD transceiver and controller.

frequency of 4 GHz for the UWB TX. This allows for receiving data like a conventional time-division multiplexing (TDM). In frequency domain, due to the wide band characteristics of the UWB, it is evident that we can use the same antenna for the RX, if the RX band resides within 3.1−10.6 GHz as shown in Fig. 2(b). In our transceiver implementation, a center frequency of 5.2 GHz has been chosen for the unlicensed national information infrastructure (U-NII) band receiver structure. By taking advantage of asymmetrical transmission in the proposed transceiver architecture, the receiver takes incoming signals in between the transmission with a lower data rate and provides 5× oversampling to enhance reliability. This B-TDD data transmission scheme can realize the real-time closed-loop control with a single antenna, without a power-hungry self-cancellation scheme between TX and RX packets.

Fig. 3 shows the top-level circuit architecture for the implementation of the B-TDD transceiver. It consists of a continuous-time U-NII band receiver, a feedforward edge combiner-based UWB transmitter, a digital controller, and a 400 MHz phase-locked loop (PLL) for the system integration. As mentioned, the operating bands of the receiver and transmitter are fully overlapped, thus one small antenna can be shared. The U-NII band receiver is designed to interface with the transmitter with a full data rate of 10 Mbps. The U-NII band receiver is comprised of a fast-switching LNA with the first stage amplification of 21 dB, a G_m stage for additional gain of 12 dB, an envelope detector (ED) to down convert the signal to baseband, a buffer stage, and a dynamic comparator for demodulation. The fast-switching LNA is a key block to realize reliable operation of the proposed B-TDD operation, which will be covered in detail in the Section III-A. For TX, our previous feed-forward edge combiner-based UWB structure [24] has been modified with additional phase chopping to enhance energy efficiency. A digital controller with a serial peripheral interface (SPI) is also implemented on-chip to handle the demodulated signal from the receiver with 5× oversampling, and to decode the signal and redistribute to the SPI for communication with the recording/stimulation module. A 400 MHz type-II PLL is adopted to generate a system clock from a 4 MHz crystal oscillator [25]. Due to the page limitation, the design of the PLL will not be described in this paper

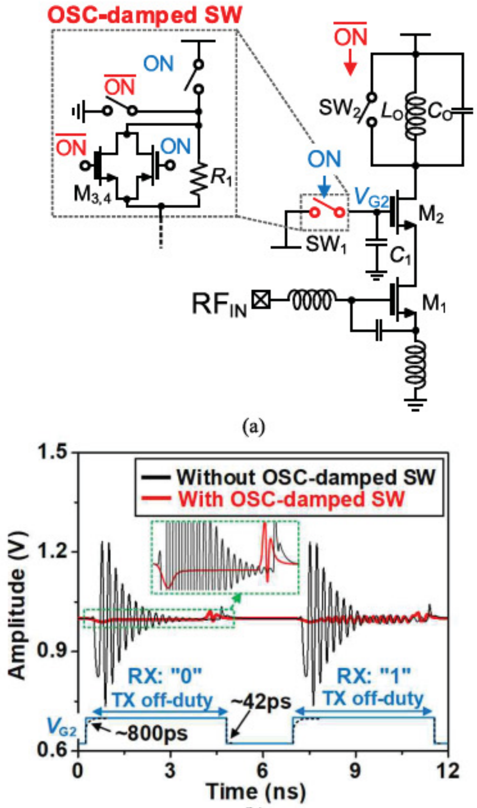

Fig. 4. (a) LNA schematic with the OSC-damped switch, and (b) Damping comparison in SPECTRE simulations.

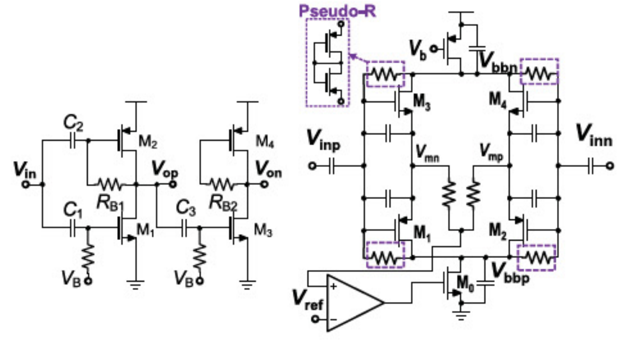

Fig. 5. (a) Self-biased single-to-differential G_m stage, and (b) Envelope detector.

III. Integrated Circuit Implementation

A. Fast Switching U-NII Band Receiver

The fast and complete switching in the LNA is a key requirement for the reliable operation of the B-TDD architecture because it guarantees a low crosstalk between the up- and downlinks, resulting in low BER. To implement such a switching in the LNA, we use two switches ($SW_{1,2}$) to control the gate bias of M_2 as well as the output tank in the LNA, as shown in Fig. 4(a). The on-and-off timings of the switches is directly correlated with the transmission signals with a delay of $<$1 ns, as shown in Fig 2(a). When the baseband sends the data to the transmitter, the data edge is forwarded to logic gates to disable the RX amplification. As soon as TX pulses are transmitted, the last edge will then active the RX to start receiving signals. With the given technology of 65 nm CMOS processes, the fast switching within 4 ns of the time slot is easily implementable. However, if the switching is too fast, particularly during on-switching, it can inject instantaneous current into the tank, resulting in prolonged ringing in a high-Q tank. Fig 4(b) shows the ringing (black line) in the output of the LNA from SPECTRE simulations. To alleviate the erroneous decision caused by the ringing, we developed an OSC-damped switch that inserts a 2.5 kΩ damping resistor (R_1) in series in the gate of M_2. While turning on the LNA, the charging path R_1–C_1 gives a larger time constant (800 ps) to smooth out the transition of current injection into the tank, consequently suppressing the ringing, as shown in the enlarged section in Fig. 4(b). In the real implementation, the time constant would not be precise as intended, however 20% error of the time constant would be good enough to suppress the ringing. On the other hand, when the edge triggers the RX switch signal to transition from short to open, the oscillation is inherently suppressed by the SW_2 in parallel with the tank. Therefore, to restore the fast operation, a transmission gate composed of $M_{3,4}$ is inserted to reduce the equivalent resistance down to $\sim$130 Ω, recovering the fast operation. In the core of LNA, a source-degeneration scheme is adopted to achieve a narrow band response in our application.

To provide additional gain in the receiver, an inverter-based, self-biased single-to-differential G_m stage is used as shown in Fig. 5(a). In ultralow power applications, an inverter-based resistive-feedback topology is popular because of its simplicity and smaller area consumption compared to LC tanks [26]–[28]. Resistive feedback, inverter-based amplifier exhibits a large gain-bandwidth product, resulting in a larger gain since the effective input transconductance becomes twice by utilizing both M_1 and M_2. As shown in Fig. 5(a), C_1 and C_2 work as decoupling capacitors to separate the bias from the previous stage, *i.e.*, LNA, while M_1 is biased via an additional current source set by V_B and M_2 uses a resistive feedback to set the gate biasing point. The output of the first stage will then be forwarded to the gate of M_3 through a decoupling capacitor C_3 and further amplified to produce a differential output for envelope detector (ED).

To provide a differential input for the ED, an extra stage to produce a 180-degree phase shift is also implemented through M_3, M_4 and R_{B2}. Note that v_{G3} is equal to v_{on}. After further amplification in the G_m stage, the received signals are sent to the ED differentially. The ED circuit is shown in Fig. 5(b). It takes advantage of the drain current behavior when biased in weak inversion [28]. We have chosen this ED structure because it provides extra gain compared to conventional passive RC filter. When biased in weak inversion, the current of the input transistor pairs ($M_{1\text{-}4}$) can be written as (1) [28], [29]:

$$I_d = I_0 e^{\frac{v_G - V_{th}}{nV_T}} \left(e^{-\frac{v_S}{V_T}} e^{-\frac{V_i^+}{V_T}} - e^{-\frac{v_D}{V_T}} \right) \approx I_Q e^{\frac{-v_i^+}{V_T}} \quad (1)$$

where $I_Q = I_0 \cdot \exp[(v_G - V_{th})/n\underline{V}_T] \cdot \exp(-v_S/V_T)$, V_T is the thermal voltage, V_{th} is the threshold voltage, and n represents a

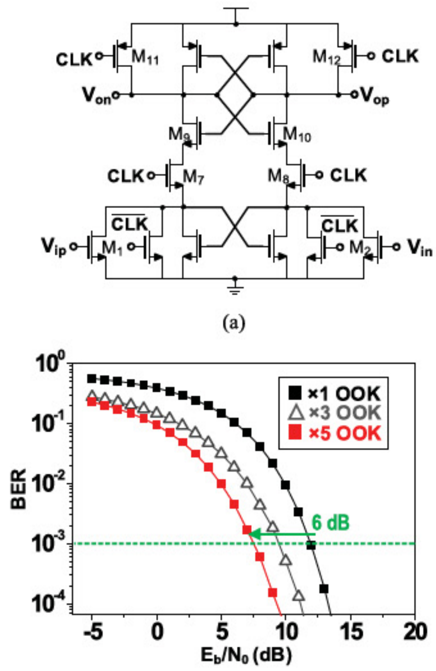

(a)

(b)

Fig. 6. (a) Dynamic comparator and (b) BER vs. OSR demodulation.

correction factor in the slope of transfer functions for losses due to capacitive division. The power series expansion of (2) can be written as:

$$I_d = I_Q \left[1 + \left(\frac{-v_i^+}{V_T} \right) + \frac{1}{2!} \left(\frac{-v_i^+}{V_T} \right)^2 + \frac{1}{3!} \left(\frac{-v_i^+}{V_T} \right)^3 + \ldots \right] \tag{2}$$

If the input signal is written as a single tone sine wave, $v_i{}^+ = \mathrm{A}\sin(2\pi.f_{\mathrm{in}}.t)$, then the 2nd-order term of (2) becomes:

$$I_d \approx \frac{I_Q A^2}{4V_T^2} \left[1 - \cos\left(2\pi \cdot 2f_{in} \right) t \right] \tag{3}$$

From (3), the DC term can be obtained while the $2f_{\mathrm{in}}$ term can be easily filtered out. With the differential structure shown in Fig. 5(b), the differential output voltage ($v_{\mathrm{on}} = v_{\mathrm{mp}} - v_{\mathrm{mm}}$) can then be expressed as:

$$v_{on} = -\frac{I_Q A^2 R_{out}}{2V_T^2} \tag{4}$$

while R_{out} is the output resistance seen at the node. The received RF signal is fed into both gate and source of transistors (*e.g.*, $\mathrm{M}_{3,4}$) to provide a twice gain before squared and low pass filtered to extract the envelope. To provide a differential output, the bottom part of the ED is the mirrored structure by adopting PMOS transistors ($\mathrm{M}_{1,2}$) and a common-mode feedback current source M_0 to define the operating point. With the same analysis method, v_{op} can be easily obtained.

The down-converted signal is buffered and demodulated by a dynamic comparator. A two crossed-coupled pair structure has been employed for the dynamic comparator as shown in Fig. 6(a). When CLK = low, $\mathrm{M}_{11,12}$ drag the output nodes to the supply, while $\mathrm{M}_{7,8}$ are shut off, leaving no constant current flowing to either branches. In the meantime, $\mathrm{M}_{3,4}$ drag the drain of the input pair to ground for a clean reset. When CLK switches from low to high, the difference at the drains of input transistors gets positively reinforced and further discharges the output node v_{op} and v_{on} at a different rate due to the voltage difference between the input pair. The output latches further enhance the output difference until one of $\mathrm{M}_{9,10}$ is turned off, and the comparison process is completed. The transition current also gets shut off once the comparison is completed; so no static power is consumed. During the emission of transmitting signals, the switch pairs in the LNA turn off amplification, which may lead to approximately 20% of signal power loss in receiving the data when compared to the continuous time operation, assuming the transmitter is operating at its full speed. To compensate for this loss, the comparator oversamples 5× at 50 MHz and the demodulated data will be sent to a voting circuit block in a digital controller to determine its final output.

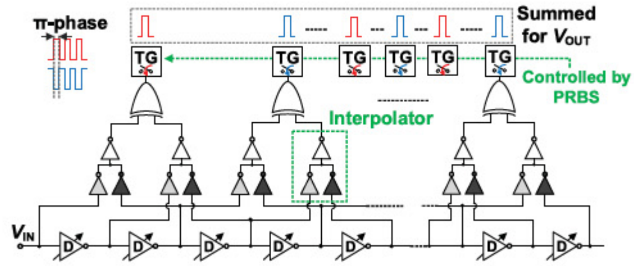

Fig. 7. Random delay frequency hopping edge combiner-based pulse generator.

B. Winner-Take-All Voting Scheme

With RX sampling at 50 MHz, the 5× oversampled data in the dynamic comparator is sent to the digital controller for winner-take-all voting. The voting system will output the demodulated 1-b result based on the majority poll among 5 incoming data. The voting scheme can improve the BER performance by 6 dB at 0.1% error rate compared to the case without the voting from SPECTRE simulations, as shown in Fig. 6(b).

C. Overlap-Free Frequency Hopping Transmitter

For TX, we modified our previous feed-forward edge combiner-based circuit [24]. The simplified conceptual diagram of overlapping-free, frequency-hopping (FH) pulse generators is shown in Fig. 7. In the UWB TX, the generated pulses with regular repetition rates generate the undesirable spectrum of transmitting signals, called “spectral (or comb) lines,” limiting the maximum transmittable power. To address this issue, we adopted the randomly delayed pulses used in DB-BPSK [30]. This scheme allows the UWB transmitter to emit higher power without violating the federal communications commission (FCC) mask, and the communicating distance can be improved by utilizing a FH technique [31]. To implement this scheme, the generated pulses are separated into two groups: red and blue pulses in Fig. 7. With the randomly selected on/off transmission gates (TGs) by the 7-bit pseudorandom binary sequence (PRBS) generator, it produces a pulse train which has

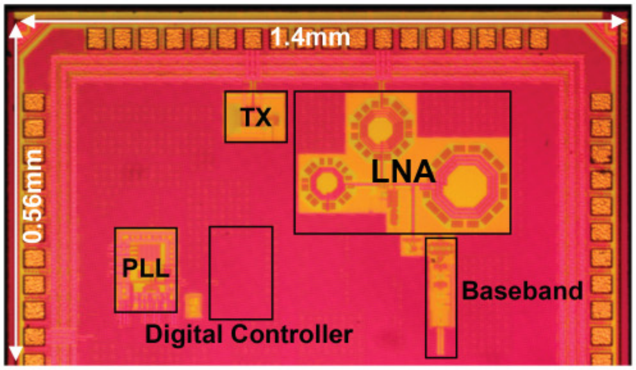

Fig. 8. A microphotograph of the fabricated transceiver chip.

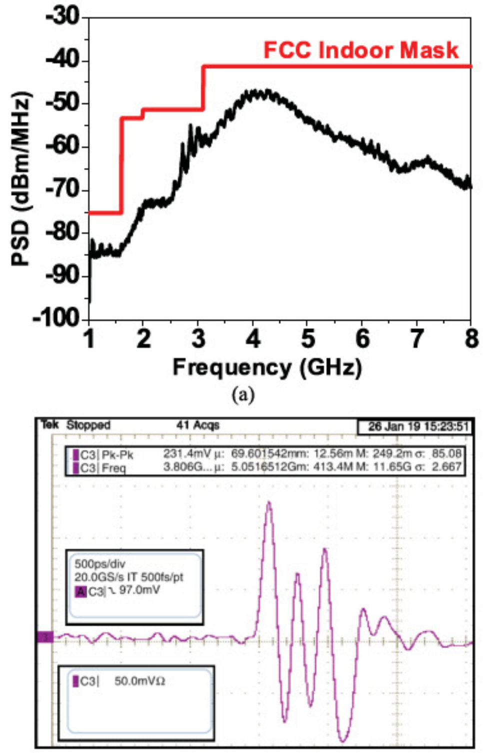

Fig. 9. (a) UWB PSD at a data rate of 200Mbps and (b) Snapshot of the enlarged transmitted waveform.

a phase delay of π between the transmitted signals, achieving the random delay between pulse sets. A frequency hopping scheme is also implemented with a variable delay cell chain, by adjusting the current course in each delay cell [24].

D. Digital Controller

To communicate with the base station and AFE module, a digital controller was also implemented in the transceiver chip. When the module is first initialized, a known serial pattern is sent to the chip with a phase delay. From this, the transceiver chip can capture the correct timing, since the demodulated signal is oversampled at 50 MHz. After this synchronization is completed, the digital controller sets up the recording and stimulation channel parameters based on the header of each bit stream. Once the recording channels are all set, the controller will repeat the command for the stimulation channels. To communicate with the stimulation and recording AFE module [18], two sets of SPI buses are implemented in the controller. The SPI clocks (SCLK) are derived from the 400 MHz PLL while the enable signals are activated based on the header of the received signal. Aside from the communication signals with the recording and stimulation AFE module, the controller also controls the hopping and random delays in the transmitter to eliminate the comb lines and enable high emission power up to 0 dBm.

IV. Experiment Results

The transceiver chip was fabricated in a 65 nm RF CMOS process. The fabricated chip microphotograph is shown in Fig. 8. The chip area is 1.4×0.56 mm^2 including pads, while the core area is less than 0.35 mm^2.

A. Benchtop Wireless Module Validation

Fig. 9(a) shows the power spectral density (PSD) of the UWB transmitter. The PSD is under the FCC indoor mask at 200 Mbps where pseudorandom binary sequence (PRBS) trains are generated from frequency hopping and a random delayed scheme. The pulse overlapping is prevented; so there is no peak at half the transmitting frequency, 2.4GHz. Fig. 9(b) shows the enlarged transmitted waveform with P_{out} of -8 dBm and a carrier frequency of 4.8GHz. Fig. 10(a) shows the

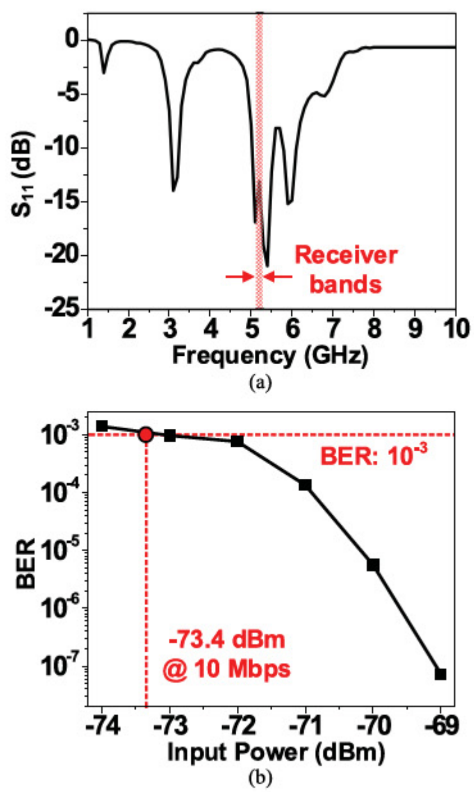

Fig. 10. Receiver characteristics: (a) Input S_{11}, (b) BER vs input power.

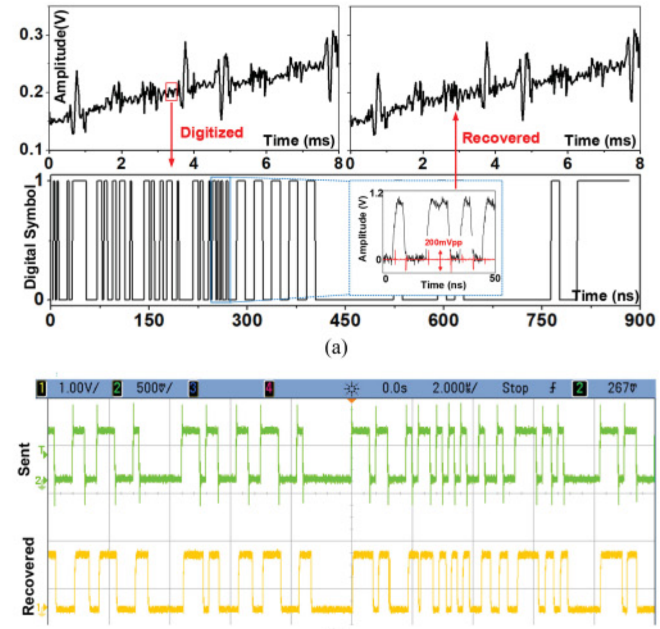

Fig. 11. Transient waveforms: (a) in the transmitter and (b) in the receiver with pre-recorded neural signals.

input matching (S_{11}) of the receiver LNA. The value is under -10 dB at the band of interest (5.15–5.25GHz). The BER is shown as a function of input power in Fig. 10(b). The detectable input power with $< 0.1\%$ BER is –73.4 dBm at 10 Mbps. The time-domain performance of the fabricated B-TDD transceiver has been characterized. Fig. 11(a) shows the transient waveform of the fragmented digitized signals from the pre-recorded neural signal sent to the transmitter. The transmitter output pulses are generated when the input signals toggle, as shown in the inset of Fig. 11(a). The recovered and demodulated waveforms from the receiver are shown in Fig. 11(b) at 10 Mbps. The performance of the fabricated transceiver is compared with the other state-of-the-art works in Table I. Our work achieved a high data rate of 200 Mbps from a relatively lower power consumption thanks to the devised B-TDD scheme that does not require power-hungry SIC circuits, resulting in decent energy efficiencies in both up- and down-links, 9.7 pJ/b and 0.32 nJ/b respectively, while allowing high output power emission. The works in [20] and [31] showed better energy-efficiencies than ours but their output power emissions are limited because of insufficient TX/RX isolations. Our implementation also does not require any additional passive filters nor duplexers at the input/output of the transceiver, thereby the overall system can be compact. In addition, our transceiver chip contains all the digital control functions and clock generation, which further reduces complexity in system integration and operation for *in vivo* experiments.

B. Prototype System Integration and in-vivo Validation

A prototype wireless bidirectional optogenetic system is implemented to verify the full functionalities and performance of the B-TDD transceiver. The integrated prototype system is shown in Fig. 12. The system used a commercially available optoelectrode with 12 μLEDs and 32 recording sites (μLED-12-32-F, NeuroLight Technologies, USA) [19], [21] in accordance with the functional block diagram illustrated in Fig. 1. In the future, we may be able to integrate a high-density optoelectrode which has over hundreds of recording channels and optical stimulation sites when available [35]. A custom optogenetic AFE IC with low-power 32-channel electrical recording and 12-channel pulse-shaping optical stimulation [19] was assembled with the fabricated B-TDD transceiver chip. Also, a few COTS components, such as a Li-battery (GM301016 TUV UL1642, PowerStream, Canada) and an antenna (ANT1085, TDK Corporation, Japan), were added. The size of the headstage PCB is 38×17 mm^2. The total system, including the battery, weighs < 5.0 grams that satisfies the weight requirement for rodent experiments ($< 10\%$ of rodent weight). The system can record, stimulate, and communicate data continuously for more than 3 hours without recharging the battery, when operating at 100 μA with 10% duty-cycled optical stimulation.

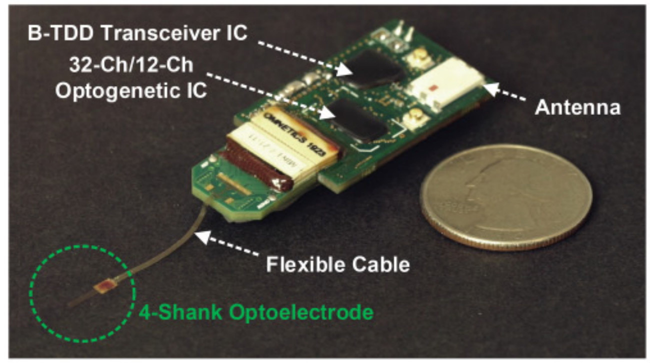

Fig. 12. Assembled optogenetic neural interface where a proposed B-TDD transceiver, a micromachined 32/12 optoelectronic probe, a 32/12 custom AFE and simulator are integrated in a miniaturized headstage [18].

In vivo experiments were carried out to validate the feasibility of the prototype wireless bidirectional optogenetic system for simultaneously recording and stimulation on a rodent. The animal procedures were approved by the Institutional Animal Care and Use Committee of the University of Michigan IACUC (protocol number: PRO-7275). One male C57BL/6J mouse (32 g) and one transgenic male mouse (JAX stock #007612) were used in this study. The mice were kept on a regular 12 h–12 h light–dark cycle and housed in pairs before surgery. No prior experimentation had been performed on these animals. AAV5, CaMKII promoter driven channel rhodopsin-2 (ChR2, AAV5-CaMKIIa-hChR2(H134R)-EYFP) virus was injected in CA1 region of the hippocampus of the wild type of mouse, resulting in expression of ChR2 in pyramidal neurons. Atropine (0.05 mg/kg, s.c.) was administered after isoflurane anesthesia induction to reduce saliva production. The body temperature was monitored and kept constant at 36–37 °C with a DC temperature controller (TCAT-LV; Physitemp, Clifton, NJ, USA). Stages of anesthesia were maintained by confirming the lack of nociceptive reflex. Skin of the head was shaved, and the

TABLE I
PERFORMANCE COMPARISON OF DUPLEX TRANSCEIVER SYSTEMS

	Publication year	This work	2011 [12]	2015 [21]	2020 [22]	2016 [31]	[32]	2017 [34]
	Technology (nm)	**65**	65	65	130	180	N/A	65
	Frequency (GHz)	**5.2/UWB**	0.8-1.4	0.1-1.5	0.915	2.4/UWB	2.4	1.0-1.8
	Duplex Scheme	**[a]Bit-wise TDD**	FD/FDD	FDD	TDD	FDD	[b]Packet-wise TDD	FDD
	Isolation Technique	**Fast-switching LNA**	Integrated RF filters	Passive mixer first	Switch Controlled	TX spectrum shaping	Switching LNA	Cancellation DAC
TX	Data rate (Mbps)	**200**	25	20	2.5	2	500	20
	Max P_{out} (dBm)	**[c]-3**	[e]15	[e]-15	-30.6	-18-0	[d]-60/[e]-10	12.6
	Power (mW)	**1.94**	N/A	N/A	0.0482	33.8	3.5	0.4
	FoM (pJ/b)	**9.7**	N/A	N/A	19.28	16900	7	845
RX	Modulation	**OOK**	QAM	N/A	OOK	N/A	OOK	N/A
	Data rate (Mbps)	**10**	25	6-192	0.1	0.25-2	100	20
	Power (mW)	**3.2**	63-69(RX) + 138 (Canceller)	[f]43-56	0.0275	40.5	5	40 (RX)+ 60 (DAC)
	FoM (nJ/b)	**0.32**	8.28	[g]0.29	0.275	20.25	0.05	5
	Sensitivity(dBm)	**-73.4**	[h]-86	[h]-81.2	-69	-82	-79.9	[h]-79.7
	Antenna Size (cm^2)	**[i]1 × 0.8**	N/A (a pair)	[j]5 × 0.9	10.2 × 10.2	1 × 1	1.5 × 1.65	[j]5 × 0.9
	Integration level	**Fully integrated**	RX + LO + Canceller	RF frontend + LO gen.	Rf frontend + RF-DC	External clk. + controller	Fully integrated	External clk. + controller
	Passive filter	**Not required**	Required	Not Required	Not Required	Required	Required	Not Required
	Die Area (mm^2)	**0.35**	4.8	1.5	1.4	0.8	N/A	3.9

[a]switching time <1 ns
[b]switching time $= 130\ \mu s$
[c]without external self-interference cancellation
[d]estimated with noise figure, bandwidth, BER, and isolation
[e]requires digital backend self-interference cancellation of >50dB [39]
[f]full chip
[g](full chip power)/(RX BW)
[h]BER < 10-3
[i]Commercial antenna used
[j]PulseLarsen, W1903

surface of the skull was cleaned by hydrogen peroxide (2%). A 1 mm diameter craniotomy was drilled at 1.5 mm posterior removed over the dorsal CA1 region and virus was injected. Viruses were purchased from the University of North Carolina Vector Core [36]. After the surgery, the craniotomy was sealed with Kwik-Sil (World Precision Instruments) until the day of recording. On the day of recording, mice were anesthetized with isoflurane, the craniotomy was cleaned (virus injected animal) or prepared (transgenic animal) and the µLED optoelectrode was lowered to the CA1 region of the hippocampus. 15 min length of simultaneous recording and stimulation were performed using one µLED from on shank (all µLEDs were tested at least once). The AFE on the headstage was used to record signals (n = 32 channels) and to deliver current pulses (n = 12 µLEDs). The recorded data were analyzed by custom scripts written in MATLAB (MathWorks, USA). Offline, spikes were detected and automatically sorted using the Kilosort algorithm followed by manual curation using Phy to get well-isolated single units (multi-unit and noise clusters were discarded). To measure the effect of LED stimulation on neuronal activity, peristimulus time histograms (PSTHs) were built around stimulus onset (spike trains were binned into 10-ms bins). Baseline and light-induced firing rate were calculated for each single unit. Baseline was defined as light-free epochs (500 ms) between trials and stimulation period as the light was on (5000 ms). Wilcoxon-signed rank test was used to compare the mean firing rate per trial (n = 43 trials) during baseline and LED stimulation.

The distance between the on-PCB transceiver and the fabricated on-chip transceiver is 1 meter in the setup. The *in vivo* result in transient is shown in Fig. 13, 13(a) and (b) show the direct output from the frontend circuit and the retrieved signal from base station, respectively. 100 µA, 1 Hz with 50% duty cycle current is applied for µLED optical stimulation. With one meter of distance, the retrieved BER maintains < 0.1%. Fig. 14(a) shows the location of µLED probe in the *in-vivo* testing setup. The electrode was lowered to the CA1 region of the hippocampus where LED-2 on shank 3 was turned on at 100 µA, 1 second period and 30% duty cycle. Fig. 14(b) shows the raw signal recorded on shank 3. 2 trials of the light induced neuronal effects are shown, the effect is highlighted in red. Light induced artifacts are also present in the raw data at stimulation onset and offset. Fig. 15(a) shows the details of shank 3 of the µLED probe. Note that LED-2 was illuminated during the example trances. Fig. 15(b) shows the high pass filtered signal of Fig. 14(b) where 4th order Butterworth filter with 600 Hz cutoff corner is applied. Light-induced activity is highlighted in red. Table II shows the comparison of this work to the other recent wireless bidirectional systems. This prototype wireless bidirectional optogenetic achieves the smallest size and weight with low power consumption among the state-of-the-art

TABLE II
COMPARISON OF WIRELESS BIDIRECTIONAL OPTOGENETIC SYSTEMS

Publication year		**This work**	2020 [20]	2020 [37]	2018 [38]
Technology (nm)		**65 (RF) 180 (Rec, Stim)**	350	180 & COTS (Stim)	130 & COTS (RF)
Bidirectional communication method		**B-TDD**	FDD	TDM	TDM
Power source		**Li-battery**	Inductive link	Li-battery	LiPo-battery
System size (mm^2)		**38 × 17**	70 × 50	43 × 20	–
System weight (g)		**4.9**	17	6	–
Number of recording channels		**32**	16	2	10
Number of stimulation channels		**12**	16 (Optical) 8 (Electrical)	1 (Optical) 1 (Electrical)	4
Recording	Bandwidth (Hz)	**1–10k**	(1–100) – 10k	0.05–187.5	0.5–7k
	Resolution (bit)	**10**	10	8.5[1]	9.8[1]
	IRN (μV_{rms})	**5.7**	3.5	1.3	3.2
	Power/Channel (μW)	**23.6**	50	14.5	11.2
Optical Stimulation	Current range (mA)	**0-1**	0.8-24.8	0-120	0-35
	Resolution (bit)	**10**	5	4	N/A
	Modulation	**Arbitrary**	Exponential decay	PWM	PWM
	Power/Channel (μW)	**31**	137.5	–	–

[1]ADC ENOB

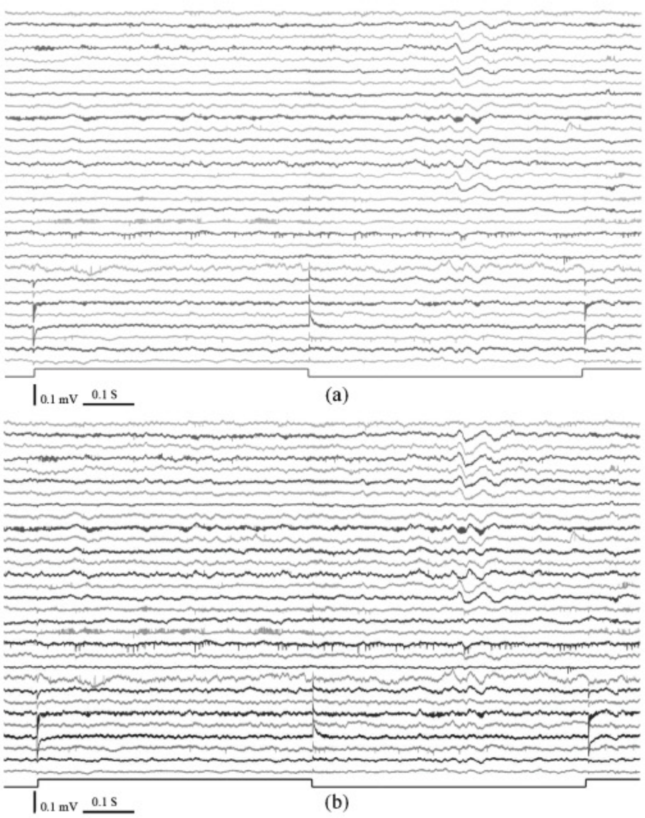

Fig. 13. In vivo testing result: (a) Direct output from the AFE chip and (b) Recovered signal from base station (transceiver output).

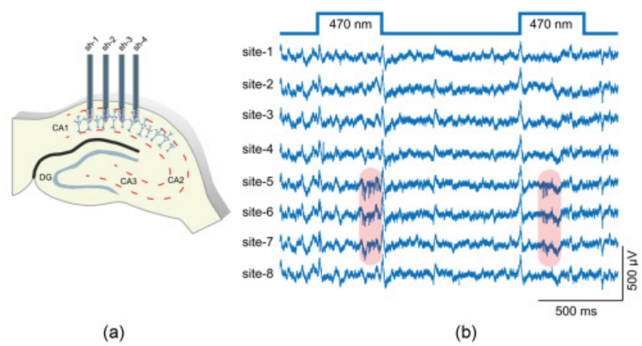

Fig. 14. (a) Location of the μLED probe and (b) Raw signals on shank 3.

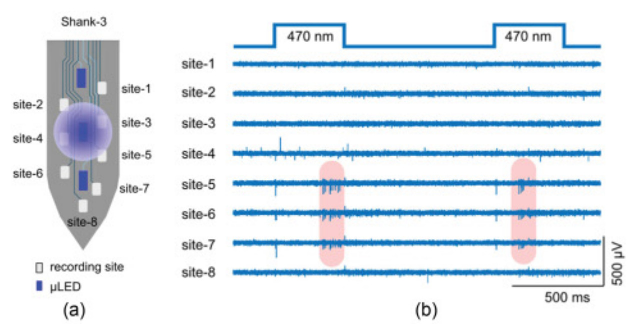

Fig. 15. (a) Details of shank 3 and (b) High pass filtered signal.

works, demonstrating that it is suitable for *in vivo* experiments in freely behaving animals. In addition, considering the high bandwidth allocated for the proposed transceiver, one can easily extend the implementation for higher channel-count wireless neural recording and modulation systems (with pulse shaping functions) without much extra cost and effort [35], which is essential to enable the advancement of neuroscience research for mapping the local circuit network connections in the brain.

V. CONCLUSION

In this paper, we presented a full integration of B-TDD wireless data telemetry for implantable broadband optogenetic neural modulation and recording platform. The B-TDD transceiver utilizes both ultra-wide band and U-NII band to achieve one-antenna solution without power-hungry self-interference cancellation scheme. Data loss due to slow switching between receiving and transmitting is also avoided by adapting the bit-wise switching scheme as well as the asymmetrical data transferring protocol. Together with pre-existing ASICs, the prototype integrated system was assembled to demonstrate the entire system with a total weight of under 5 g operating on battery power, which makes it suitable for rodent experiments. In *in vivo* experiments, the target neurons were successfully stimulated by the designated corresponding μLEDs driven by the wireless prototype system and the optically activated neural responses could be monitored in real time with $< 0.1\%$ BER through wireless data transmission.

References

[1] E. S. Boyden, F. Zhang, E. Bamberg, G. Nagel, and K. Deisseroth, "Millisecond-timescale, genetically targeted optical control of neural activity," *Nat. Neurosci.*, vol. 8, no. 9, pp. 1263–1268, 2005, doi: 10.1038/nn1525.

[2] J. Dai, D. I. Brooks, and D. L. Sheinberg, "Optogenetic and electrical microstimulation systematically bias visuospatial choice in primates," *Curr. Biol.*, vol. 24, no. 1, pp. 63–69, 2014, doi: 10.1016/j.cub.2013.11.011.

[3] P. Anikeeva *et al.*, "Optetrode: A multichannel readout for optogenetic control in freely moving mice," *Nat. Neurosci.*, vol. 15, no. 1, pp. 163–170, 2012, doi: 10.1038/nn.2992.

[4] F. Wu, E. Stark, P. C. Ku, K. D. Wise, G. Buzsaki, and E. Yoon, "Monolithically integrated μLEDs on silicon neural probes for high-resolution optogenetic studies in behaving animals," *Neuron*, vol. 88, no. 6, pp. 1136–1148, 2015, doi: 10.1016/j.neuron.2015.10.032.

[5] G. Buzsáki *et al.*, "Tools for probing local circuits: High-density silicon probes combined with optogenetics," *Neuron*, vol. 86, no. 1, pp. 92–105, 2015, doi: 10.1016/j.neuron.2015.01.028.

[6] K. N. Noh *et al.*, "Miniaturized, battery-free optofluidic systems with potential for wireless pharmacology and optogenetics," *Small*, vol. 14, no. 4, pp. 1–8, 2018, doi: 10.1002/smll.201702479.

[7] G. Shin *et al.*, "Flexible near-field wireless optoelectronics as subdermal implants for broad applications in optogenetics," *Neuron*, vol. 93, no. 3, pp. 509–521.e3, 2017, doi: 10.1016/j.neuron.2016.12.031.

[8] S. Il Park *et al.*, "Stretchable multichannel antennas in soft wireless optoelectronic implants for optogenetics," *Proc. Nat. Acad. Sci. USA*, vol. 113, no. 50, pp. E8169–E8177, 2016, doi: 10.1073/pnas.1611769113.

[9] M. L. Wang, S. Baltsavias, T. C. Chang, M. J. Weber, J. Charthad, and A. Arbabian, "Wireless data links for next-generation networked micro-implantables," in *Proc. IEEE Custom Integr. Circuits Conf.*, Apr. 2018, vol. 6, no. 1, pp. 1–9, doi: 10.1109/CICC.2018.8357096.

[10] Y. Rajavi, M. Taghivand, K. Aggarwal, A. Ma, and A. S. Y. Poon, "An RF-powered 58Mbps-TX 2.5Mbps-RX full-duplex transceiver for neural microimplants," in *Proc. IEEE Radio Freq. Integr. Circuits Symp.*, May 2016, pp. 234–237, doi: 10.1109/RFIC.2016.7508294.

[11] J. Zhou, T. H. Chuang, T. Dinc, and H. Krishnaswamy, "Integrated wideband self-interference cancellation in the RF domain for FDD and full-duplex wireless," *IEEE J. Solid-State Circuits*, vol. 50, no. 12, pp. 3015–3031, Oct. 2015, doi: 10.1109/JSSC.2015.2477043.

[12] M. Pelissier *et al.*, "A 112 Mb/s full duplex remotely-powered impulse-UWB RFID transceiver for wireless NV-memory applications," *IEEE J. Solid-State Circuits*, vol. 46, no. 4, pp. 916–927, Mar. 2011, doi: 10.1109/JSSC.2011.2110990.

[13] C. M. Lopez *et al.*, "A 966-Electrode neural probe with 384 configurable channels in 0.13 μm SOI CMOS," in *Proc. IEEE Int. Solid-State Circuits Conf.*, Jan. 2016, pp. 392–393, doi: 10.1109/ISSCC.2016.7418072.

[14] J. J. Jun *et al.*, "Fully integrated silicon probes for high-density recording of neural activity," *Nature*, vol. 551, no. 7679, pp. 232–236, 2017, doi: 10.1038/nature24636.

[15] E. Musk, "An integrated brain-machine interface platform with thousands of channels," *J. Med. Internet Res.*, vol. 21, no. 10, pp. 1–14, 2019, doi: 10.2196/16194.

[16] S.-Y. Park, J. Cho, K. Na, and E. Yoon, "Modular 128-channel Δ-$\Delta\Sigma$ analog front-end architecture using spectrum equalization scheme for 1024-Channel 3-D neural recording microsystems," *IEEE J. Solid-State Circuits*, vol. 53, no. 2, pp. 501–514, Nov. 2018, doi: 10.1109/JSSC.2017.2764053.

[17] S.-Y. Park, J. Cho, K. Lee, and E. Yoon, "Dynamic power reduction in scalable neural recording interface using spatiotemporal correlation and temporal sparsity of neural signals," *IEEE J. Solid-State Circuits*, vol. 53, no. 4, pp. 1102–1114, Jan. 2018, doi: 10.1109/JSSC.2017.2787749.

[18] S.-Y. Park *et al.*, "A miniaturized 256-channel neural recording interface with area-efficient hybrid integration of flexible probes and CMOS integrated circuits," *IEEE Trans. Biomed. Eng.*, vol. 69, no. 1, pp. 334–346, Jan. 2022, doi: 10.1109/TBME.2021.3093542.

[19] A. E. Mendrela, S.-Y. Park, M. Vöröslakos, M. P. Flynn, and E. Yoon, "A battery-powered opto-electrophysiology neural interface with artifact-preventing optical pulse shaping," in *Proc. IEEE Symp. VLSI Circuits*, Jun. 2018, pp. 125–126, doi: 10.1109/vlsic.2018.8502353.

[20] Y. Jia *et al.*, "A trimodal wireless implantable neural interface system-on-chip," *IEEE Trans. Biomed. Circuits Syst.*, vol. 14, no. 6, pp. 1207–1217, Nov. 2020, doi: 10.1109/TBCAS.2020.3037452.

[21] D. Yang, H. Yüksel, and A. Molnar, "A wideband highly integrated and widely tunable transceiver for in-band full-duplex communication," *IEEE J. Solid-State Circuits*, vol. 50, no. 5, pp. 1189–1202, Mar. 2015, doi: 10.1109/JSSC.2015.2403362.

[22] M. Cai, A. Asoodeh, Y. Luo, and S. Mirabbasi, "An ultralow-power crystal-free batteryless TDD radio for medical implantable applications," *IEEE Trans. Microw. Theory Tech.*, vol. 68, no. 11, pp. 4875–4885, Jun. 2020, doi: 10.1109/TMTT.2020.3003302.

[23] K. Kim *et al.*, "GaN-on-Si μLED optoelectrodes for high-spatiotemporal-accuracy optogenetics in freely behaving animals," in *Proc. IEEE Int. Electron. Device Meeting*, Dec. 2016, pp. 643–646, doi: 10.1109/IEDM.2016.7838486.

[24] D. D. Wentzloff and A. P. Chandrakasan, "A 47pJ/pulse 3.1-to5GHz all-digital UWB transmitter in 90nm CMOS," in *Proc. IEEE Int. Solid-State Circuits Conf.*, Feb. 2007, pp. 118–120.

[25] B. Razavi, *Design of Analog CMOS Integrated Circuits*, 2nd ed. McGraw-Hill Education International Edition.

[26] G. Chang, S. Maity, B. Chatterjee, and S. Sen, "Design considerations of a sub-50 μW receiver Front-end for implantable devices in medradio band," in *Proc. IEEE Int. Conf. VLSI Des.*, Jan. 2018, vol. 2018, pp. 329–334, doi: 10.1109/VLSID.2018.85.

[27] T. Taris, J. B. Begueret, and Y. Deval, "A 60μW LNA for 2.4 GHz wireless sensors network applications," in *Proc. Dig. Paper - IEEE Radio Freq. Integr. Circuits Symp.*, Jun. 2011, pp. 12–15, doi: 10.1109/RFIC.2011.5940633.

[28] S. Chen, C. Yang, and K. Cheng, "A 4.5 μW 2.4 GHz wake-up receiver based on complementary current-reuse RF detector," in *Proc. IEEE Int. Symp. Circuits Syst.*, May 2015, pp. 1214–1217.

[29] Y. Lin, S.-Y. Park, X. Chen, D. Wentzloff, and E. Yoon, "4.32-pJ/b, overlap-Free, feedforward edge-combiner-based ultra-wideband transmitter for high-channel-count neural recording," *IEEE Microw. Wireless Compon. Lett.*, vol. 28, no. 1, pp. 52–54, Dec. 2018.

[30] S. Geng *et al.*, "A 13.3 mw 500 Mb/s IR-UWB transceiver with link margin enhancement technique for meter-range communications," *IEEE J. Solid-State Circuits*, vol. 50, no. 3, pp. 1–10, Feb. 2015.

[31] S. A. Mirbozorgi, H. Bahrami, M. Sawan, L. A. Rusch, and B. Gosselin, "A single-chip full-duplex high speed transceiver for multi-site stimulating and recording neural implants," *IEEE Trans. Biomed. Circuits Syst.*, vol. 10, no. 3, pp. 643–653, Oct. 2016, doi: 10.1109/TBCAS.2015.2466592.

[32] Single Chip 2.4GHz Transceiver, nRF24L01, Nordic Semiconductor datasheet.

[33] M. Vidojkovic *et al.*, "A 0.33nJ/b IEEE802.15.6/proprietary-MICS/ISM-band transceiver with scalable data-rate from 11kb/s to 4.5Mb/s for medical applications," in *Proc. IEEE Int. Solid-State Circuits Conf.*, Feb. 2014, vol. 57, pp. 170–171, doi: 10.1109/ISSCC.2014.6757386.

[34] L. Calderin, S. Ramakrishnan, A. Puglielli, E. Alon, B. Nikolic, and A. M. Niknejad, "Analysis and design of integrated active cancellation transceiver for frequency division duplex systems," *IEEE J. Solid-State Circuits*, vol. 52, no. 8, pp. 2038–2054, Jun. 2017, doi: 10.1109/JSSC.2017.2700360.

[35] K. Kim *et al.*, "HectoSTAR microLED optoelectrodes for large-scale, high-precision in invo opto-electrophysiology," *bioRxiv*, 2020. [Online]. Available: https://doi.org/10.1101/2020.10.09.334227

[36] B. R. Arenkiel *et al.*, "In vivo light-induced activation of neural circuitry in transgenic mice expressing channelrhodopsin-2," *Neuron*, vol. 54, no. 2, pp. 205–218, 2007, doi: 10.1016/j.neuron.2007.03.005.

[37] S. Y. Lee *et al.*, "A programmable EEG monitoring SoC with optical and electrical stimulation for epilepsy control," *IEEE Access*, vol. 8, pp. 92196–92211, May 2020, doi: 10.1109/ACCESS.2020.2994217.

[38] G. Gagnon-Turcotte, M. N. Khiarak, C. Ethier, Y. De Koninck, and B. Gosselin, "A 0.13-μm CMOS SoC for simultaneous multichannel optogenetics and neural recording," *IEEE J. Solid-State Circuits*, vol. 53, no. 11, pp. 3087–3100, Feb. 2018, doi: 10.1109/JSSC.2018.2865474.

[39] D. Bharadia, E. McMilin, and S. Katti, "Full duplex radios," in *Proc. ACM SIGCOMM 2013 Conf. SIGCOMM*, 2013, pp. 375–386.

Yu-Ju Lin received the B.S. and M.S. degrees in electrical engineering from National Taiwan University, Taipei, Taiwan, in 2010 and 2012, respectively, and the Ph.D. degree in electrical and computer engineering from the University of Michigan, Ann Arbor, MI, USA, in 2019. In 2011, she joined Bell labs, Murray Hills, NJ, USA, as a one-year intern where she was developing mm-wave signal chain for radar application. She is currently employed with Qualcomm Atheros, San Jose, CA, USA. Her research interests include ultra-low power transceiver for biomedical applications.

Hyunsoo Song (Graduate Student Member, IEEE) received the B.S. and M.S. degrees in electrical engineering from Seoul National University, Seoul, South Korea, in 2010 and 2012, respectively. He is currently working toward the Ph.D. degree in electrical and computer engineering with the University of Michigan, Ann Arbor, MI, USA. Until 2016, he had worked for Pixelplus Co., Ltd., Suwon, South Korea, to design CMOS image sensor pixel devices. His current research focuses on CMOS image sensors embedded with low latency vision processing.

Sungjin Oh (Graduate Student Member, IEEE) received the B.S. and M.S. degrees in electrical and computer engineering from Seoul National University, Seoul, South Korea, in 2013 and 2015, respectively. He is currently working toward the Ph.D. degree in electrical and computer engineering with the University of Michigan, Ann Arbor, MI, USA. From 2015 to 2018, he was with the Korea Institute of Science and Technology as a Research Scientist. His research focuses on mixed-signal integrated circuit design for biomedical systems.

Mihály Vöröslakos received the M.D. and the Ph.D. degrees in neuroscience from the University of Szeged, Hungary, in 2016 and 2012, respectively. He is currently a Postdoctoral Researcher with New York University Langone Health's Neuroscience Institute, Buzsaki Lab, New York, NY, USA, and a Visiting Research Scholar with the University of Michigan, Yoon Lab, Ann Arbor, MI, USA. His research interests include non-invasive brain stimulation in both rodent and human models and development of useful tools for the neuroscience community.

Kanghwan Kim (Member, IEEE) received the B.E. degree in electrical engineering from The Cooper Union, New York, NY, USA, in 2013, and the M.S.E. and Ph.D. degrees in electrical engineering from the University of Michigan, Ann Arbor, MI, USA, in 2015 and 2020, respectively. He is currently with the Korea Institute of Science and Technology, Seoul, South Korea. His research interests focuses on developing tools for advanced neuroscience research, including multifunctional neural probes for optogenetics study and recording and stimulation system for real-time closed-loop neuroscience experiments in freely moving animals.

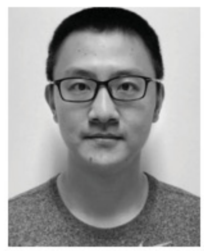

Xing Chen (Member, IEEE) received the B.S. degree from the Beijing Institute of Technology, Beijing, China, in 2013, and the M.S. degree in 2015 from the University of Michigan, Ann Arbor, MI, USA, where he is currently working toward the Ph.D. degree. In 2018, he joined Qualcomm, San Diego, CA, USA, as an RFIC Design Intern, where he was developing frequency synthesizers for 5G applications. He also held internship positions with Psikick, Inc., Charlottesville, VA, USA, in 2017, and Carnegie Mellon University, Pittsburgh, PA, USA, in 2014. His research interests include analog/mixed signal IC design, all digital frequency synthesizers for wireless communications, and energy efficient RF transceivers.

David D. Wentzloff (Senior Member, IEEE) received the B.S.E. degree in electrical engineering from the University of Michigan, Ann Arbor, MI, USA, in 1999, and the S.M. and Ph.D. degrees from the Massachusetts Institute of Technology, Cambridge, MA, USA, in 2002 and 2007, respectively. In 2012, he co-founded PsiKick, Inc., Santa Clara, CA, USA, a fabless semiconductor company developing ULP wireless SoCs. Since 2007, he has been with the University of Michigan, where he is currently an Associate Professor of electrical engineering and computer science. His research focuses on RF integrated circuits, with an emphasis on ultralow power (ULP) design. He is a Senior Member of the IEEE Circuits and Systems Society, IEEE Microwave Theory and Techniques Society, IEEE Solid-State Circuits Society, and Tau Beta Pi. He was the recipient of the 2009 DARPA Young Faculty Award, 2009–2010 Eta Kappa Nu Professor of the Year Award, 2011 digital to analog converter (DAC)/ISSCC Student Design Contest Award, 2012 IEEE Subthreshold Microelectronics Conference Best Paper Award, 2012 NSF CAREER Award, 2014 ISSCC Outstanding Forum Presenter Award, 2014–2015 Eta Kappa Nu ECE Professor of the Year Award, 2014–2015 EECS Outstanding Achievement Award, and 2015 Joel and Ruth Spira Excellence in Teaching Award. He was on the Technical Program Committee for ICUWB 2008–2010, ISLPED 2011–2015, S3S 2013–2014, and Radio Frequency Integrated Circuits Symposium (RFIC) 2013–2015. He was the Guest Editor of IEEE TRANSACTIONS ON MICROWAVE THEORY AND TECHNIQUES, *IEEE Communications Magazine*, and *Elsevier Journal of Signal Processing: Image Communication*.

György Buzsáki received the M.D. degree from the University of Pécs, Pécs, Hungary, in 1974, and the Ph.D. degree in neuroscience from the Academy of Sciences, Budapest, Hungary, in 1984.

He is the Biggs Professor of neuroscience with NYU Langone Health, New York, NY, USA. His main research focuses on neural syntax, such as, how segmentation of neural information is organized by the numerous brain rhythms to support cognitive functions.

Dr. Buzsáki is among the top 1% most-cited neuroscientists, a Member of the National Academy of Sciences, USA, and the Academiae Europaeae. He sits on the editorial boards of several leading neuroscience journals, including *Science* and *Neuron*.

Sung-Yun Park (Member, IEEE) received the B.S. degree in electrical engineering from Pusan National University, Busan, South Korea, in 2005, and the M.S. degree in electrical engineering in 2008 from the Korean Advanced Institute of Science and Technology (KAIST), Daejeon, South Korea, where he was involved in photonics device research. He continued his study in integrated circuits with Cornell University, Ithaca, NY, USA, and received the M.Eng. degree in electrical and computer engineering in 2011, and the Ph.D. degree in electrical engineering from the University of Michigan, Ann Arbor, MI, USA, in 2016. From 2008 to 2010, he was with the Fairchild Semiconductor, Bucheon, South Korea, as a Member of Technical Staff for high voltage mixed signal circuit design. He was a Research Fellow during 2016–2018 and an Assistant Research Scientist (after 2018) with the University of Michigan. In 2019, he joined the Electronics Engineering Department, the Pusan National University, Busan, South Korea, where he is an Assistant Professor. His current research interests include low power, low noise mixed-signal integrated circuits and power management circuits for biomedical and sensor systems.

Euisik Yoon (Fellow, IEEE) received the B.S. and M.S. degrees in electronics engineering from Seoul National University, Seoul, South Korea, in 1982 and 1984, respectively, and the Ph.D. degree in electrical engineering from the University of Michigan, Ann Arbor, MI, USA, in 1990. From 1990 to 1994, he was with the National Semiconductor Corp., Santa Clara, CA, USA. From 1994 to 1996, he was the Technical Staff Member with Silicon Graphics Inc., Mountain View, CA, USA. He took faculty positions with the Department of Electrical Engineering, the Korea Advanced Institute of Science and Technology (KAIST), Daejeon, South Korea, during 1996–2005, and with the Department of Electrical and Computer Engineering, University of Minnesota, Minneapolis, MN, USA, during 2005–2008. During the academic year of 2000–2001, he was a Visiting Faculty with the Agilent Laboratory, Palo Alto, CA, USA. In 2008, he joined the Department of Electrical Engineering and Computer Science with the University of Michigan, where he is a Professor and the Director of the NSF International Program for Advancement of Neurotechnology (IPAN). His current research interests include MEMS, integrated microsystems, and VLSI circuit design. Dr. Yoon was on various Technical Program Committees, including the Microprocesses and Nanotechnology Conference 1998, International Sensor Conference 2001, IEEE Asia–Pacific Conference on Advanced System Integrated Circuits 2001 and 2002, International Conference on Solid-State Sensors, Actuators and Microsystems (Transducers) 2003, 2005, IEEE International Electron Device Meeting 2006–2008, and IEEE International Conference on Micro Electro Mechanical Systems 2006, 2009, and 2010. He was also on the IEEE International Solid-State Circuit Conference program committee during 2003–2007 and was the General Chair of International Symposium on Bio Micro & Nanosystems 2005. Recently, he was an Associate Editor for IEEE SOLID-STATE CIRCUIT LETTERS during 2018–2021.